Journal of Hydrology 580 (2020) 124257

Contents lists available at ScienceDirect

Journal of Hydrology

journal homepage: www.elsevier.com/locate/jhydrol

Research papers

Investigating karst aquifers: Using pseudo 3-D electrical resistivity tomography to identify major karst features

Patrizio Torrese

Dipartimento di Scienze della Terra e dell'Ambiente, Università di Pavia, Via Ferrata 9, 27100 Pavia, Italy

ARTICLE INFO

This manuscript was handled by Corrado Corradini, Editor-in-Chief, with the assistance of Barbara Mahler, Associate Editor

Keywords:
Hydrogeological Experimental Site of Poitiers
Karst aquifer
ERT
Pseudo 3-D resistivity tomography

ABSTRACT

This work presents the electrical resistivity imaging of the Hydrogeological Experimental Site (HES) karst aquifer of Poitiers (France) from pseudo three-dimensional (3-D) Electrical Resistivity Tomography (ERT), i.e., a three-dimensional model obtained from the joint inversion of resistivity data collected along parallel profiles. The inverse resistivity model provided a fairly reliable definition of the main hydrogeological units. The survey also allowed the recognition of possible shallow dissolution-enlarged fractures that do not show any ground expression at present but have been revealed at depth by vertical flowmeter data and high-resolution video footage from wells. These features seem to connect with middle-depth sub-vertical features down to a depth of 25 m, which are likely to correlate with soil-mantled, incipient sinkhole formation features that do not show any ground expression at present, as well as karst conduits. At greater depth, the resistivity model allowed the recognition of the first two main karst intervals (35–40 m and 85–87 m deep) associated with water productive layers, as revealed by well logs. The opportunity to cross-validate geophysical results with extensive ground truth provided by the HES allowed an assessment of the error the pseudo 3-D ERT model makes in estimating the depth of the karst intervals. Synthetic dataset modelling provided the detectability of the pseudo 3-D ERT model in identifying karst intervals. Synthetic dataset modelling also allowed an estimation of the response of the experimental and inversion setup to a variable degree of heterogeneity of the aquifer, using well-log data as geological *a priori* information.

1. Introduction

Electrical Resistivity Tomography (ERT) is a proven imaging technique where the theory (cf. Arato et al., 2014; Athanasiou et al., 2007; Buvat et al., 2013; Dahlin and Loke, 1998; Daily and Owen, 1991; Loke et al., 2003; Spiegel et al., 1980) and application (cf. Cassiani et al., 2009; Daily and Ramirez, 1992; Griffiths and Barker, 1993; Guérin and Benderitter, 1995; Guérin et al., 2004; Kuras et al., 2009; Ritz et al., 1999) are well-documented in geophysical literature. ERT is a technique well-suited to identifying karst features and it partially characterizes karst aquifers. Karst features can be predominantly air-filled, making them highly resistive (e.g., > 1000 Ω·m), or partially or completely water-filled (e.g., 60–1000 Ω·m); in the latter case, depending on the ionic concentration of the groundwater, karst features may have a bulk conductivity ranging from very conductive (e.g., 60–100 Ω·m) to relatively conductive (e.g., 100–250 Ω·m), compared to the host rock (e.g., > 2000 Ω·m for not karst limestone). Karst features may also be filled by highly-weathered material, such as clays, in which case they will be conductive relative to the host rock (e.g., 60–150 Ω·m).

There have been many applications of electrical resistivity methods to detect karst features, sinkholes and cavities, see, for instance, Al-Zoubi et al., 2007; Carrière et al., 2013; Maillol et al., 1999; Rainone et al., 2015; Satitpittakul et al., 2013; Smith, 1986; Van Schoor, 2002; Zhu et al., 2011. Meyerhoff et al. (2012, 2014) show the application of time-lapse ERT to study changes of electrical conductivity in karst aquifers during times of varying discharge.

This work presents the electrical resistivity imaging of the Hydrogeological Experimental Site (HES) karst aquifer of Poitiers (France, Poitou-Charentes region) from pseudo three-dimensional (3-D) ERT. This is a 3-D model obtained from the joint inversion (not simply 2-D data interpolation) of resistivity data collected along parallel profiles. The target of the study is to provide further insights into the applicability and effectiveness of pseudo 3-D ERT in karst aquifer investigation at relatively great depth, down to 100 m. Better accuracy may be obtained from actual 3-D ERT surveys (i.e., data actually collected along the three directions, rather than pseudo 3-D surveys) but, at these depths, the pseudo 3-D survey is often an enforced choice due to the significant use of field equipment (i.e., very long multi-core cables) that a 3-D ERT survey would involve.

The main geophysical targets of this study are represented by karst

E-mail address: patrizio.torrese@unipv.it.

https://doi.org/10.1016/j.jhydrol.2019.124257
Received 17 August 2019; Received in revised form 4 October 2019; Accepted 17 October 2019
Available online 18 October 2019

intervals, i.e., zones of void development as identified by well logs. The opportunity to cross-validate geophysical results with extensive ground truth provided by the HES allowed an evaluation of the accuracy of the pseudo 3-D model and the effectiveness of some of the most common surface electrode arrays in investigating difficult geological targets such as karst aquifers.

The detectability of karst intervals provided by the pseudo 3-D ERT model was assessed through synthetic dataset modelling, i.e., a numerical simulation aimed at evaluating the capacity of the implemented pseudo 3-D ERT survey to detect predefined targets at the HES. Well-log data available from the dense well network at the HES were used as geological *a priori* input information for the generation of synthetic models (SYMs) representing different features of the HES aquifer. Therefore, the synthetic datasets produced by forward modelling, through the application of the SYMs, were inverted to generate synthetic dataset models to be compared with field dataset models. This approach allowed an estimation of the response of the experimental and inversion setup to a variable degree of heterogeneity of the aquifer and guided the interpretation of field data.

1.1. Geological setting of the test site

The HES of Poitiers is located on the southern border of the Paris Basin (Fig. 1a). In this region, Jurassic limestone outcrops or lays beneath a thin cover of Tertiary clays (Fig. S1 in the Supporting Information) and is slightly tilted toward the north. This monoclinic structure is cut by sub-vertical faults from several tectonic phases between the Eocene and Pliocene epochs (Burbaud-Vergneaud, 1987; Delay et al., 2004, 2007; Kaczmaryk and Delay, 2007a,b) with the development to the south of horst structures like those of Seuil du Poitou and Ligugé. Jurassic aquifers are therefore sub-horizontal limestone and vertically fractured along the N–S and E–W directions. The Hercynian crystalline basement underlies the Jurassic limestone (Fig. S1 in the Supporting Information).

1.2. The hydrogeological experimental Site (HES)

The HES of Poitiers (Fig. 1a,b) was developed by the Institut de Chimie des Milieux et des Matériaux de Poitiers (University of Poitiers and French National Center for Scientific Research) within the Network of National Hydrogeological Sites (SNO H+). The HES is found on the Seuil du Poitou, a large Mesozoic carbonate plateau marking the transition between the Aquitaine and Paris sedimentary basins. The HES is located in one of the main regional aquifers, which includes: (i) the Lower and Middle Lias Aquifer (5 to 10 m thick) and (ii) the Dogger Aquifer (approximately 100 m thick). These aquifers are hydraulically separated by the marly Toarcian aquitard (20 m thick). An argillaceous limestone, approximately 30 m thick, overlies the Dogger aquifer, indicating that the Dogger Aquifer is sealed beneath this thick, relatively impermeable formation.

Thirty-five fully penetrating open wells were drilled with destructive techniques, using a down-the-hole (DTH) hammer/rotary, until the top of Toarcian marls located at a depth of approximately 125 m (Fig. 1b). All the holes completely traverse the Dogger Aquifer. These wells were cased with a 0.24 m diameter steel pipe to depths ranging from 15 to 80 m. Below the steel casing, some wells were uncased while others were partly or fully screened with a 0.17 m diameter machine-slotted PVC pipe. Most of the wells were arranged according to a regular grid in a square area measuring 210 × 210 m, according to a multiscale nested five-spot pattern (Audouin et al., 2008, their Fig. 2). This pattern is classically used in petroleum engineering to improve oil recovery by simultaneously injecting water into the corner wells and pumping oil in the central well. This technique was used at the HES to optimize the tracer recovery during tracer tests and to provide an experimental facility for flow and transport upscaling studies. A large volume of data was collected from the Dogger Aquifer. These data, stored in the H + database (De Dreuzy et al., 2006) include: the geologic structure of the reservoir (Bourbiaux et al., 2007), well logs (Audouin, 2007), petrophysical properties, porosity and permeability measurements (Bourbiaux et al., 2007), flow conditions in the boreholes (Audouin et al., 2008), water-table dynamics (Audouin, 2007; Audouin & Bodin, 2007, 2008; Bernard & Delay, 2008; Bernard et al., 2006; Delay et al. 2004; Delay et al. 2007; Kaczmaryk & Delay 2007a,b), and the 3-D seismic imaging of the reservoir (Mari & Porel, 2008a).

Under natural flow conditions, the piezometric level (that measured in the boreholes which are screened/open hole over the entire length of the aquifer, represents the average hydraulic head over the thickness of the aquifer) varies from 20 m to 25 m below ground level (bgl). However, due to heavy rainfall, a piezometric level of 17 m bgl was observed during ERT data collection.

The aquifer is highly heterogeneous, with local variations in both lithology and fracture density, as revealed by the correlation between natural gamma and long normal resistivity logs (Audouin et al., 2008, their Fig. 5), the 3-D porosity block achieved by 3-D seismic surveys (Mari & Porel, 2008b), and the variability in borehole yields that range from less than 5 m^3/h to > 60 m^3/h. The boreholes with higher yields are those which intercept at least one karst feature. Vertical flowmeter data and high-resolution photography reveal two sets of fractures-fissures: a main set that is NW-SE oriented and a minor N-S oriented set. There are also three different main karst intervals (i.e., zones of void development) at depths of 35–40 m, 85–87 m and 110–115 m (Audouin et al., 2008); these were also confirmed by stratigraphic and resistivity well logs. Heat-pulse flowmeter logs and borehole imaging analyses show that inflow levels are associated to sub-horizontal karst structures, which are confined within vuggy limestone layers. These vuggy levels are well marked by dark shades on borehole images (Audouin et al., 2008, their Fig. 10). A net increase in macroscopic porosity is associated to the localized presence of dissolution cavities 1–3 cm in diameter.

The vertical interconnectivity between the three karst intervals seems to result from sub-vertical fracture occurrence, as revealed by borehole imaging. Fractures are either isolated or concentrated within fracture zones. No large cavities have been intercepted by wells. However, the presence of sub-vertical conduits or cavities of a significant size cannot be excluded considering that sub-vertical features are under sampled by the vertical wells.

Karst intervals (water-filled) lead to a fall in the resistivity of the Dogger Limestone. An example of stratigraphic and resistivity logs for well M04 is shown in Fig. 2. Cross-sections of well logs have been shown by Audouin et al. (2008, their Figs. 5 and 10).

2. Materials and methods

2.1. Field dataset collection

ERT field data were collected between 17 and 22 June 2013 at the HES with a fully-automatic multi-electrode resistivity meter: the SYSCAL Jr Switch-48 by IRIS Instruments (400 V max output voltage, 1200 mA max output current, 100 W max output power). ERT data were collected using a Wenner-Schlumberger (WS) array, which delivers high vertical resolution and signal amplitude, and a Pole–Dipole (PD) array that shows high lateral resolution and penetration depth and, even if it is more susceptible to noise contamination, may present a good compromise between resolution and signal strength (Smith, 1986). In accordance with Szalai et al. (2009), who report that it is worth combining and jointly inverting data obtained with arrays differing in depth of investigation and resolution, a hybrid array sequence was obtained by merging WS and PD array sequences.

The acquisition layout comprised of 48 electrodes at 10 m intervals along five, parallel, 470 m-long surface profiles (ERT 1-ERT 5) and with each profile approximately 50 m apart. The PD array comprised of a

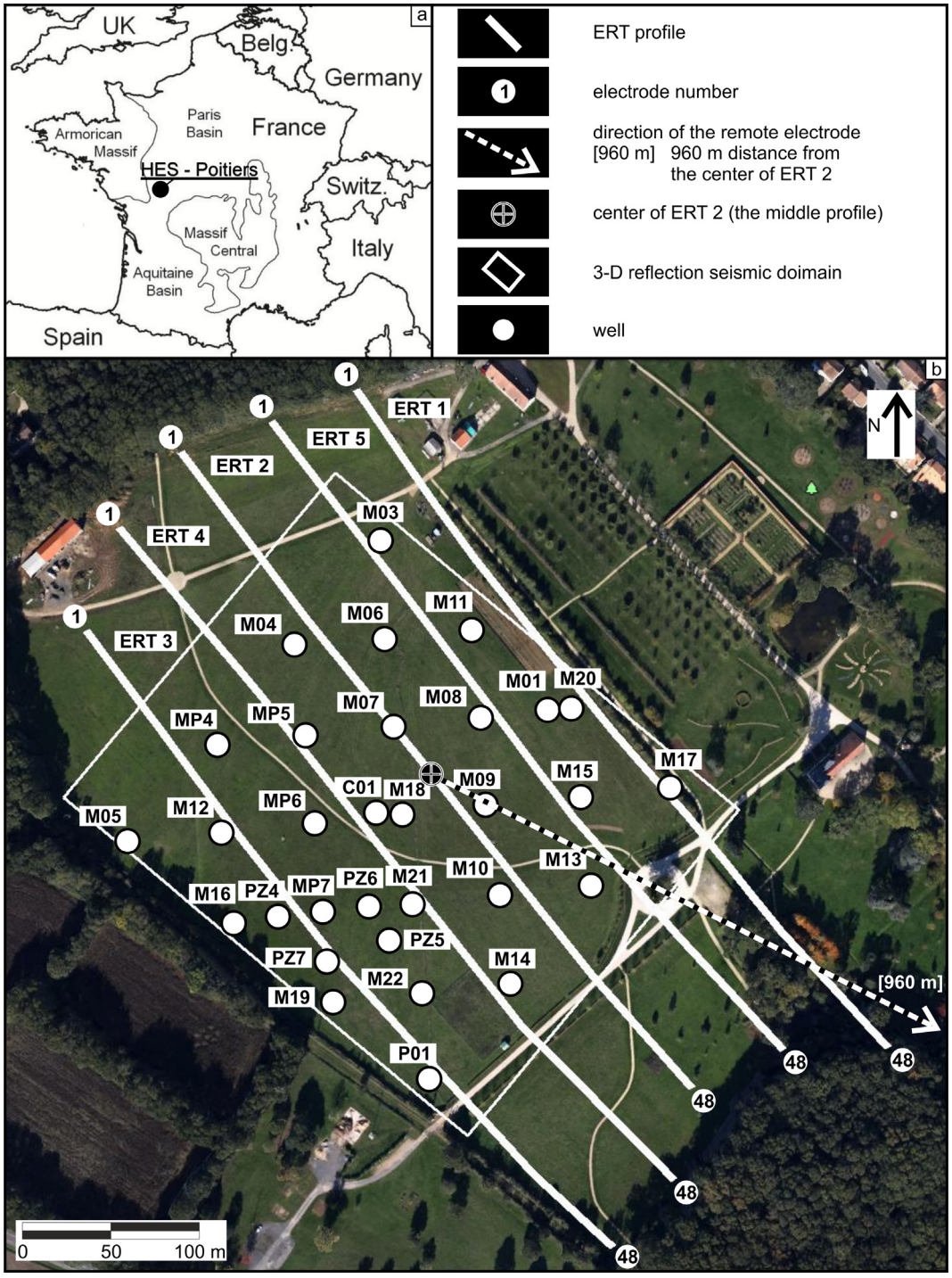

Fig. 1. (a) Geographical setting and (b) experimental layout of the HES of Poitiers. The remote electrode is located outside the area specified in b.

remote electrode at a distance of 960 m from the center of the 3-D block (Fig. 1b). The quadrupole sequence for each profile comprised of 596 measurements for the WS array and 699 measurements for the PD array. The hybrid array sequence comprised of 1,295 measurements for each profile.

Three-dimensional resistivity grids 481 m × 203 m in size, with a maximum depth ranging from 90 m for the WS array and 130 m for the PD, were designed for merging 2-D ERT data. Details on field dataset collection are provided in Text S1 (in the Supporting Information).

Pseudo-sections reveal six intervals of apparent resistivity which represent different hydrogeological units, including the two karst intervals (Fig. S2 in the Supporting Information); the third karst interval is not detectable due to its depth, which is greater than the ERT survey's maximum depth of investigation. Some erratic measurements seem to be related to the presence of a small, very shallow, buried body. This body, acting as source of noise, is able to affect electrical resistivity measures and generates a severe measure artifact, i.e., the pant-leg anomaly shown by the pseudo-section in Fig. S2a. This anomaly is not due to the steel pipes all the wells are cased with, to depths ranging from 15 to 80 m. This finding is consistent with the results of resistivity surveys by other authors that did not record any noise due to the metallic casing from water wells located in the near vicinity of the surveys, unlike self-potential surveys (see, for instance, Saribudak and Hawkins, 2019). However, the pant-leg anomaly shown by the pseudo-section in

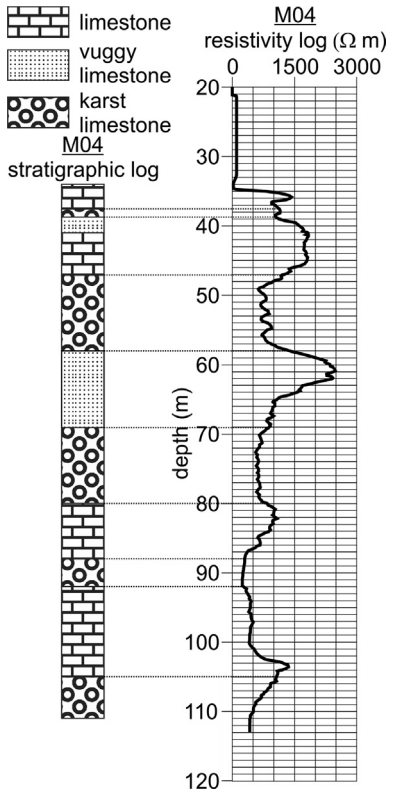

Fig. 2. Stratigraphic and resistivity logs of well M04: karst intervals (water-filled) lead to a fall in resistivity of the Dogger Limestone.

Fig. S2a was partially removed by data processing before inversion, as shown in Fig. S2b.

2.2. Processing and inversion of the field dataset

To verify the field dataset's capability to identify karst intervals, 1-D resistivity soundings were extracted from ERT apparent resistivity data (Fig. S3 in the Supporting Information). This approach allowed the verification that the first two karst intervals were correlated to an overall decrease in apparent resistivity.

Data processing allowed outliers from apparent resistivity data to be removed. Problematic data showing unrealistically high resistivity (> 600 Ω·m), too-high standard deviation (> 10 Ω·m) and negative resistivity that is unrealistic for 2-D data, were removed from apparent data.

The pseudo 3-D resistivity imaging was obtained from the joint inversion of merged 2-D ERT data. ERTLab Solver (by Multi-Phase Technologies LLC, Geostudi Astier srl), based on tetrahedral Finite Element Modelling (FEM), was used for data inversion. A tetrahedral discretization was used in both forward and inverse modelling. The foreground region was discretized using a 27.1 m element size, i.e., the weighted average of the electrode separation (due to different electrode spacing along the X and Y directions on the ground). The background region was discretized using an increasing element size towards the outside of the domain, according to the sequence 1 ×, 1 ×, 2 ×, 4 × and 8 × the foreground element size.

The forward modelling was performed using mixed-boundary conditions (Dirichlet-Neumann) and a tolerance (stop criterion) of 1.0E-7 for a Symmetric Successive Over-Relaxation Conjugate Gradient (SSORCG) iterative solver. Data inversion was based on a least squares smoothness constrained approach (LaBrecque et al., 1996). Noise was appropriately managed using a data-weighting algorithm (Morelli and LaBrecque, 1996) that allows the variance matrix after each iteration for data points poorly fitted by the model to be adaptively changed. The inverse modelling was performed using a maximum number of internal inverse Preconditioned Conjugate Gradient (PCG) iterations of 5 and a

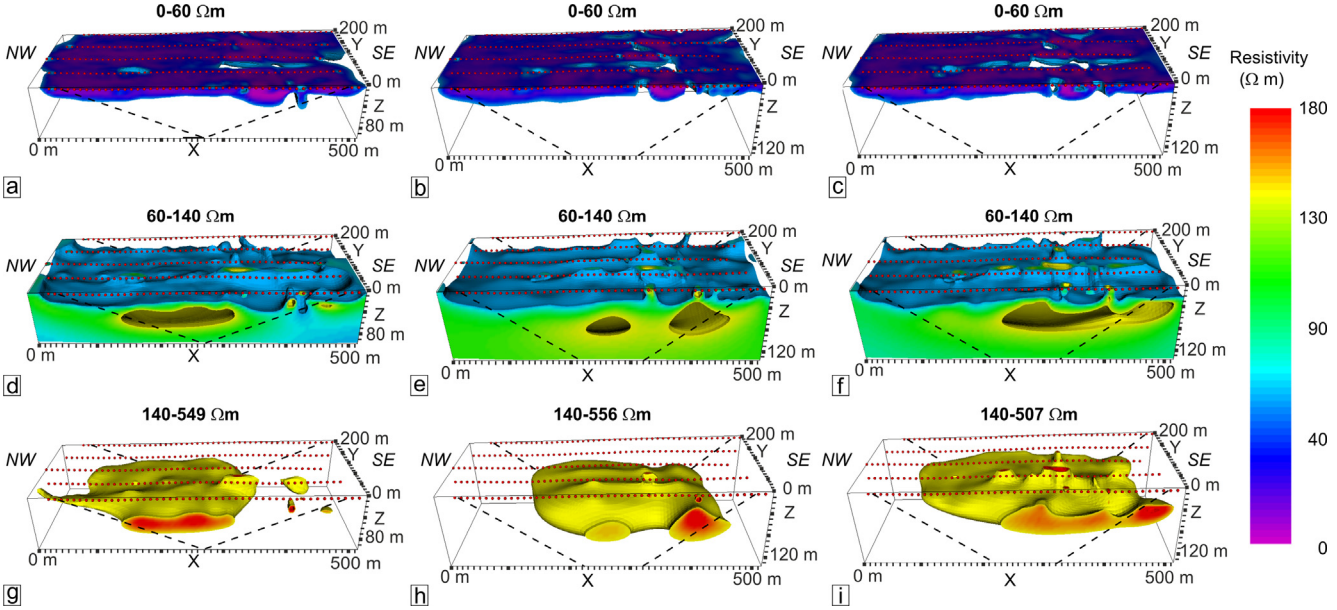

Fig. 3. Perspective view of different resistivity range extractions from pseudo 3-D inverse resistivity blocks obtained from the field dataset: argillaceous limestone affected by a main NW-SE oriented and a minor N-S oriented set of dissolution-enlarged fractures shown by (a) WS, (b) PD, (c) hybrid array models; high-porosity Dogger Limestone (also limestone affected by some clay content) affected by dissolution-enlarged fractures and karst conduits/zones of void development on its top shown by (d) WS, (e) PD, (f) hybrid array models; low-porosity Dogger Limestone affected by karst conduits/zones of void development shown by (g) WS, (h) PD, (i) hybrid array models. The red dots and the black dashed lines included in the models represent the electrodes and the limit of data from the survey, respectively. Black shadows represent the innermost regions of the model. (For interpretation of the references to colour in this figure legend, the reader is referred to the web version of this article.)

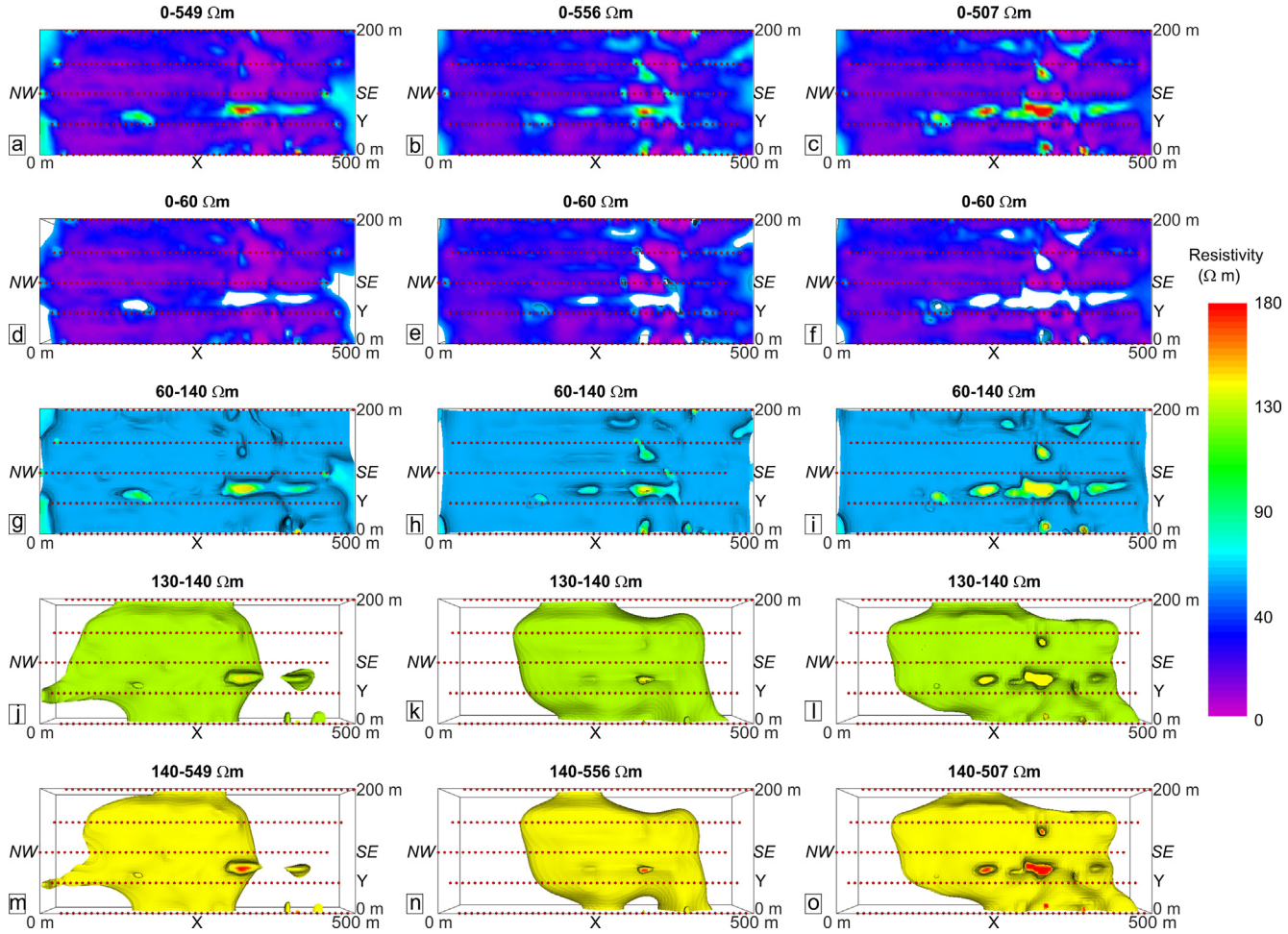

Fig. 4. Plan view of different resistivity range extractions from pseudo 3-D inverse resistivity blocks obtained from the field dataset: whole karst-system shown by (a) WS, (b) PD, (c) hybrid array models; argillaceous limestone affected by a main NW-SE oriented and a minor N-S oriented set of dissolution-enlarged fractures shown by (d) WS, (e) PD, (f) hybrid array models; high-porosity Dogger Limestone (also limestone affected by some clay content) affected by dissolution-enlarged fractures and karst conduits/zones of void development on its top shown by (g) WS, (h) PD, (i) hybrid array models; karst conduits/zones of void development and intervals shown by (j) WS, (k) PD, (l) hybrid array models; low-porosity Dogger Limestone affected by karst conduits/zones of void development shown by (m) WS, (n) PD, (o) hybrid array models. The red dots included in the models represent the electrodes. (For interpretation of the references to colour in this figure legend, the reader is referred to the web version of this article.)

tolerance (stop criterion) for inverse PCG iterations of 0.001. The amount of roughness from one iteration to the next was controlled in order to assess maximum layering: a low value of reweight constant (0.1) was set with the objective of generating maximum heterogeneity.

The inverse resistivity models (Figs. 3–5 and Fig. S4 in the Supporting Information) were obtained through the application of homogeneous starting models that set each node the average apparent resistivity value measured by the corresponding array sequence (54 Ω·m for WS, 109 Ω·m for PD, 77 Ω·m for hybrid). The inverse final resistivity models were chosen with a criterion based on the achievement of a minimum data residual (misfit error).

2.3. Method used to compare observed stratigraphy and ERT results

To quantify the differences between the directly-observed stratigraphy from the wells and the remotely-sensed stratigraphy with the ERT surveys, a comparison between available stratigraphic logs and resistivity imaging was carried out. The depth of karst intervals, defined as zones of void development revealed by stratigraphic logs, was compared to the depth where the pseudo 3-D ERT model revealed a resistivity range that was consistent with the presence of karst intervals.

The results of the comparison were returned in terms of the success rate of the ERT model in detecting karst intervals, the 3-D visual inspection and a scatter plot. As regards the success rate assessment, for instance, 50% success meant that the pseudo 3-D ERT model was able to correctly detect karst intervals in 50% of cases. The visual comparison consists in plotting the depth of karst intervals detected by the stratigraphic logs on the 3-D geophysical model. The scatter plot compares the depth at which each karst interval was detected by stratigraphic logs and by the pseudo 3-D ERT.

2.4. Synthetic dataset modelling

The same electrode arrays, quadrupole sequences and experimental setup involved in the field dataset collection were used in the synthetic dataset modelling. The same solver and inversion procedure run in the field dataset inversion were used in the synthetic dataset modelling. The only exception was the discretization of the foreground region using a 12.4 m element size along the X and Y directions and a 5.14 m element size along the Z direction. This domain discretization was necessary to prevent the occurrence of aliasing issues when applying heterogeneous synthetic models (SYMs).

Synthetic datasets were generated by forward modelling through the application of different 3-D SYMs with a variable degree of heterogeneity:

- a low-degree of heterogeneity: Layered synthetic model (SYM)

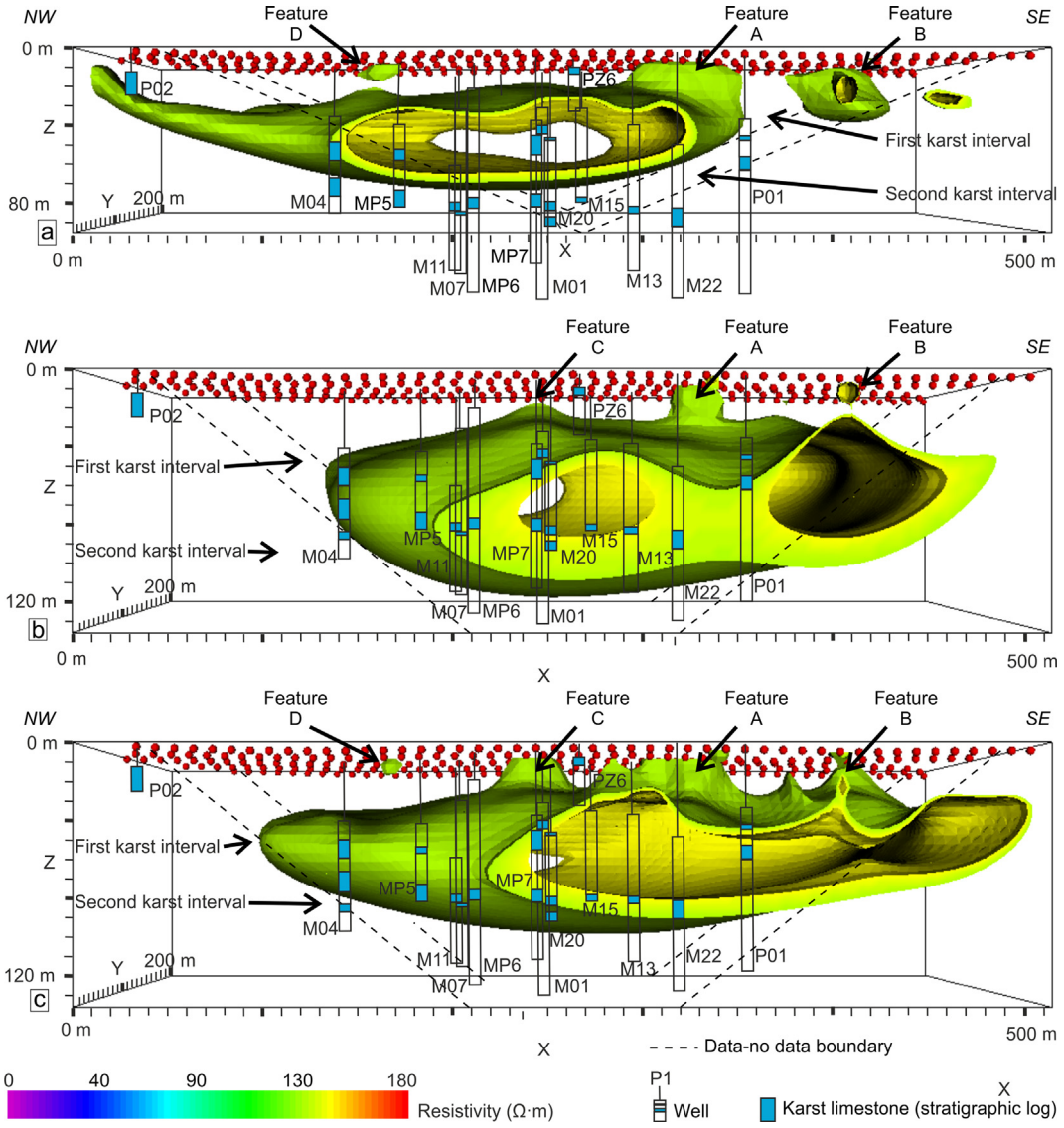

Fig. 5. Pseudo 3-D inverse resistivity models obtained from the field dataset: extraction of the 130–140 Ω·m resistivity range shown by (a) WS, (b) PD, (c) hybrid array models: this resistivity range seems to reproduce a better imaging of the first two main karst intervals occurring at depths of approximately 35–40 m and 85–87 m, as indicated by stratigraphic logs, and shallow, sub-vertical features that are likely to correlate with soil-mantled, incipient sinkhole formation features (A-D feature in the figure) and high-porosity zones. The hybrid model (and partly the PD) shows a better correlation with respect to stratigraphic logs, unlike WS, in identifying karst intervals (which are represented as light blue colored intervals). The red dots and the black dashed lines included in the models represent the electrodes and the limit of data from the survey, respectively. Black shadows represent the innermost regions of the model. (For interpretation of the references to colour in this figure legend, the reader is referred to the web version of this article.)

(Fig. 6a) simulating only the fundamental features of the aquifer; it includes 8 layers and comprises a 40 Ω·m argillaceous limestone, 2570 Ω·m not karst intervals and 745 Ω·m karst intervals: the resistivity of the bodies is the mean resistivity value observed from well resistivity logs;

- a high-degree of heterogeneity: Full Data SYM (Fig. 6b) designed by using all the information available from resistivity and stratigraphic logs of the 21 calibration boreholes (Fig. 6b): the resistivity of the bodies is the same as the Layered SYM;

- a middle-degree of heterogeneity: Smooth Full Data SYM (Fig. 6c) in order to reduce the level of detail, to eliminate spurious noise within the model and bring out regional trends; a smoothing filter (that sets each node of the SYM to the average of itself − 168 nodes immediately surrounding it and 169 nodes immediately above and below it - i.e., a filter with a 60 m size along both the X and Y direction and a 10 m size along the Z direction) was applied to the Full Data SYM to obtain from it a best-fitting smooth SYM;

- a high-degree of heterogeneity: Seismic-based SYM (Fig. 6d) obtained from a 3D reflection seismic block (Mari and Porel, 2008a,b; Mari and Delay, 2011) and comprising the same resistivity values as the Layered and the Full Data SYMs: this SYM introduced the geometry of the bodies revealed by a high resolution 3-D reflection seismic survey. The 3-D seismic block used to design the Seismic-based SYM was 300 m × 240 m in size (Fig. 1b) with a depth ranging between 32 m and 117 m.

The synthetic datasets generated by forward modelling through the application of all the SYMs were corrupted with 1% random noise to provide realistic results and were inverted to generate inverse resistivity models.

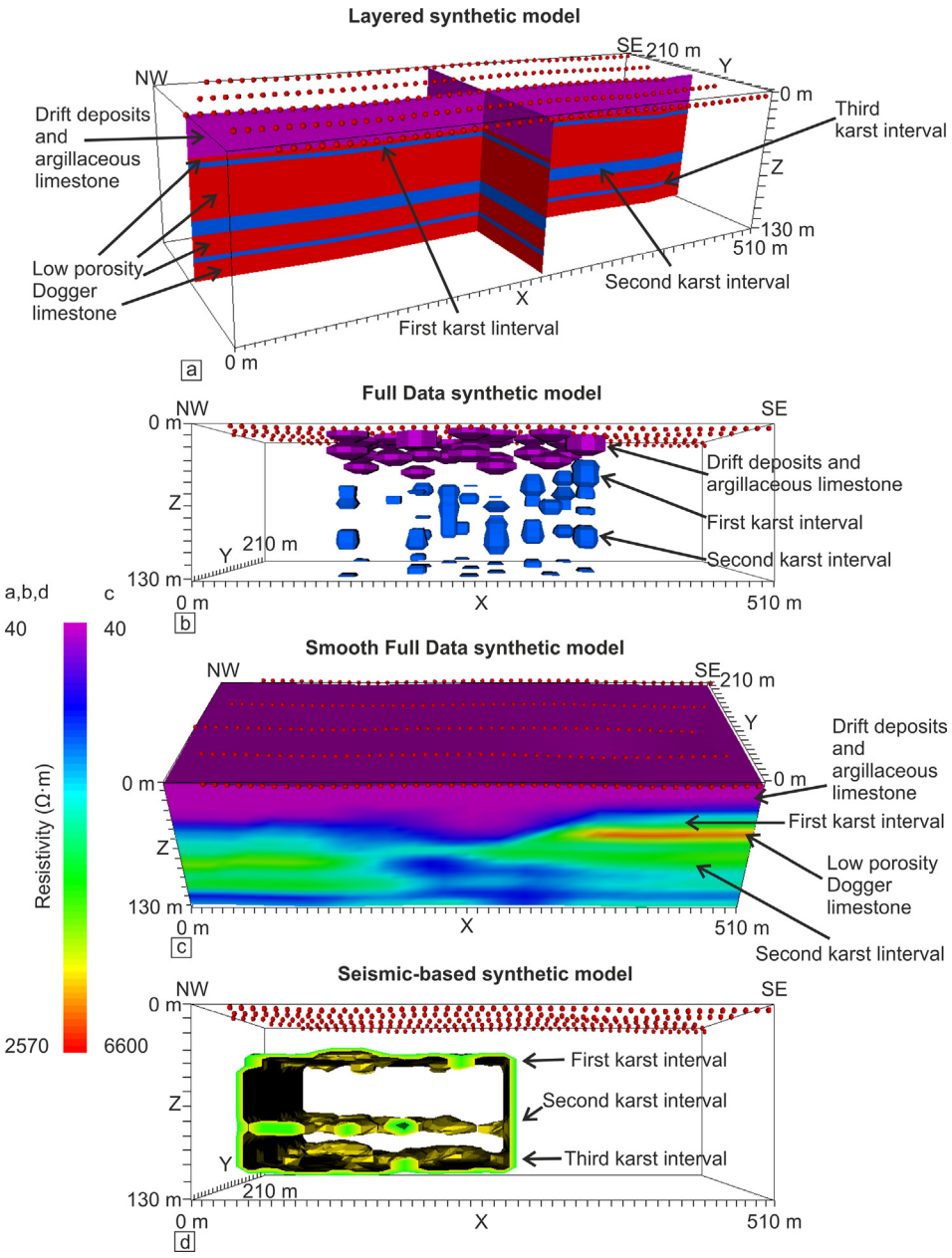

Fig. 6. 3-D synthetic models (SYMs), with a variable degree of heterogeneity, that simulate the HES karst aquifer and were used to generate realistic synthetic datasets: (a) a low-degree of heterogeneity Layered synthetic model (SYM); (b) a high-degree of heterogeneity Full Data SYM; (c) a middle-degree of heterogeneity Smooth Full Data SYM; (d) a high-degree of heterogeneity Seismic-based SYM; the SYMs were displayed using (a) fence plot, (b) log plot (c) all-voxels plot, (d) all-voxels plot on selected range visualizations of the 3-D models. The red dots included in the models represent the electrodes. Black shadows represent the innermost regions of the model. (For interpretation of the references to colour in this figure legend, the reader is referred to the web version of this article.)

3. Results

3.1. The resistivity imaging of the HES karst aquifer

Results analysis reveals an overall congruence between cross-sections and slices extracted from the pseudo 3-D models (Fig. S4 in the Supporting Information) and between pseudo 3-D models from different arrays (Figs. 3-5). Comparison between cross-sections and pseudo 3-D models reveals that the low porosity Dogger Limestone has slightly lower resistivity values in the cross-sections than in the corresponding slices extracted from the pseudo 3-D model, as shown by Fig. S4.

Three resistivity ranges can be found in the pseudo 3-D models (Figs. 3 and 4): 0–60 Ω·m for drift deposits and argillaceous limestone, 60–140 Ω·m for high-porosity Dogger Limestone (also limestone affected by some clay content), and 140–540 Ω·m for low porosity Dogger Limestone.

Argillaceous limestone (0–60 Ω·m) seems to be affected by a main NW-SE oriented trend and a minor N-S oriented trend of opening cracks (Fig. 3a-c and Fig. 4d-f) that appear to be high-resistivity structures (60–140 Ω·m) compared to host argillaceous limestone. These features may be related to shallow dissolution-enlarged fractures that do not show any ground expression at present but were revealed at depth by vertical flowmeter data and high-resolution video footage from wells.

Shallow dissolution-enlarged fractures seem to be in connection with middle-depth sub-vertical features (Figs. 3d-f, Figs. 4g-i). Further, the latter features are found within argillaceous limestone, down to a depth of 25 m, and appear to be high-resistivity structures (> 130 Ω·m) compared to the host rock. This suggests that these structures are related to void-rich zones. The 130–140 Ω·m resistivity range (Figs. 4j-l, Fig. 5) recovers a better imaging of these sub-vertical features that are likely to correlate with conduits. Larger features may be related to soil mantled, incipient sinkhole formation features that do not show any ground expression at present. At least four main incipient sinkhole formation features were recognizable (A-D feature in Fig. 5). Features A and B were revealed by all three arrays, while C was detected by PD and hybrid arrays and D was revealed by WS and hybrid arrays (Fig. 5).

The 130–140 Ω·m resistivity range (Fig. 4j-l, Fig. 5) observed from

the hybrid inverse model (and partly from the PD model) seems apparently to reproduce a better imaging of the first two main karst intervals (at a depth of approximately 35–40 m and 85–87 m) associated with water productive layers, as revealed by well logs. The third karst interval is not detectable due to its greater depth. The hybrid inverse model (Figs. 4l, Fig. 5c) is 85.7% consistent with stratigraphic logs in identifying karst intervals. The conjunction of the two karst intervals at the edges of the model seems to be due to the decrease in the density of measured data at the model's boundary. Therefore, these lateral zones should not be related to any actual hydrogeological body.

Details on the misfit of field dataset models are provided in Text S2 (in the Supporting Information).

3.2. Comparison between the HES imaging from different arrays

Although the models achieved by different array sequences are quite consistent in identifying karst intervals, represented by the same resistivity range extractions (Fig. 5), it is possible to identify some differences between them: the WS array showed a tendency to identify layering, to locate karst intervals at a shallower location and to laterally extend the bodies; the PD array sequence showed larger lateral heterogeneities and more compact and vertically-extended bodies; the hybrid array sequence delivered a better correlation with respect to stratigraphic logs (Fig. 5) despite lower data fitting (as PD). A fair congruence between the resistivity values achieved by the hybrid and the PD models is found in the 10–22 m low-depth range (within the shallow conductive layer) and in the 62–88 m high-depth range; the hybrid model delivered slightly larger values in the 22–88 m middle-depth range where the largest vertical and lateral resistivity variations occur and WS and PD array sequences are affected by different vertical and lateral resolutions.

The evidence that the hybrid array sequence delivered better imaging suggests that is worth combining and jointly inverting data obtained with arrays that differ in depth of investigation and resolution.

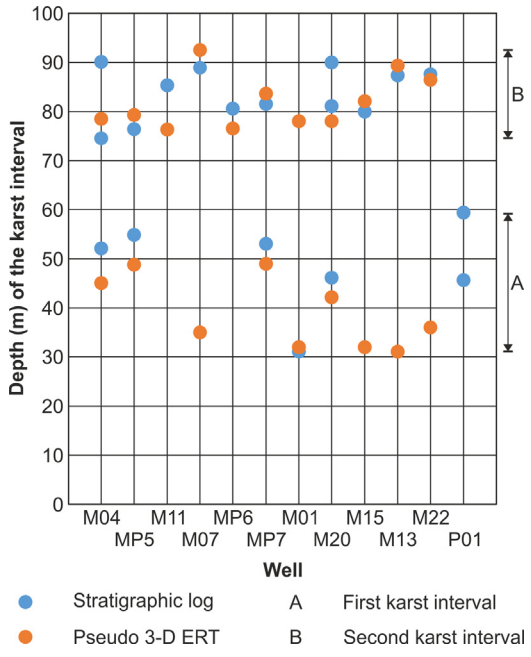

Fig. 7. Scatter plot showing the difference between the pseudo 3-D ERT hybrid model and the stratigraphic logs in estimating the depth of the karst intervals. The plot shows that the pseudo 3-D ERT is not always capable of identifying karst levels at wells M04, M20 and P01; conversely, the pseudo 3-D ERT erroneously identifies the presence of a karst level at the wells M07, M01, M15, M13, M22.

3.3. Comparison between observed stratigraphy and ERT results

The pseudo 3-D ERT model, in particular the hybrid model, is in close agreement with stratigraphic logs in identifying karst intervals. In fact, as seen before, the hybrid model, which delivered better imaging (Fig. 4l, Fig. 5c), is 85.7% consistent with stratigraphic logs in identifying karst intervals. The scatter plot in Fig. 7 shows that the difference between the pseudo 3-D ERT hybrid model and the stratigraphic logs in estimating the depth of the karst intervals ranges between −9 m and +4 m, with an average of −1.4 m and a standard deviation of 4.2 m. These findings suggest that the pseudo 3-D ERT hybrid model provides, on average, an overall slight underestimation of the depth of the karst intervals. This estimate excludes the cases in which karst intervals were not identified by either survey. In fact, there are three cases in which the karst interval is detected only by the stratigraphic log (wells M04, M20, P01) while there are five cases in which the karst interval is detected only by the pseudo 3-D ERT (wells M07, M01, M15, M13, M22). In addition, there are two cases (wells M01 and M22) in which stratigraphic logs and the pseudo 3-D ERT almost completely agree.

3.4. Detectability of karst intervals and model accuracy from synthetic dataset modelling

On the basis of synthetically-calculated data generated from the Layered SYM (Fig. 6a), by changing the thickness of the karst intervals and visually comparing the predefined SYM with the resulting image (Fig. 8a), the detectability of ERT models appears to be 4 m at a depth of 35 m (first karst interval) and 12 m at a depth of 85 m (second karst interval) for the 3-D inverse hybrid model. The PD array seems to deliver a detectability comparable to the hybrid array and about twice that of the WS array.

Synthetic dataset modelling also allowed the verification that the experimental and inversion setup involved in generating the pseudo 3-D model is capable of resolving a degree of heterogeneity comparable to that shown by the Smooth Full Data SYM model (Fig. 8c). Indeed, as revealed by the comparison between observed stratigraphy and ERT results, this model is 78.6% consistent with stratigraphic logs in identifying karst intervals. This consistency value is close to that obtained from the field dataset model (85.7%). In contrast, the Full Data SYM model (Fig. 8b, 57.2% consistent) and the Seismic-based SYM (Fig. 8d, 54% consistent) are affected by too high a degree of heterogeneity, while the Layered SYM model (Fig. 8a, 28.6% consistent) shows a degree of heterogeneity lower than the accuracy provided by the experimental and inversion setup.

Details on the misfit of synthetic dataset models are provided in Text S3 (in the Supporting Information).

4. Discussion

The pseudo 3-D ERT model provided a fairly reliable definition of the main hydrogeological units and structures such as karst intervals, possible shallow dissolution-enlarged fractures and likely soil-mantled, incipient sinkhole formation features at the HES of Poitiers. These findings, along with the assessment of the detectability developed by the experimental setup and inversion procedure used in this work, as determined by synthetic modelling, may provide further insights on pseudo 3-D ERT applicability and effectiveness in karst aquifer investigation. Better accuracy may be obtained from actual 3-D ERT surveys, but, as mentioned in the Introduction, such depths of investigation (≈100 m) would involve a significant field equipment effort.

A limit to the accuracy of the pseudo 3-D model is that, if merging not very dense 2-D profiles, the area below a 2-D profile does not really affect measurements from neighboring 2-D profiles. This means that the resulting pseudo 3-D model is driven mostly from the smoothness along

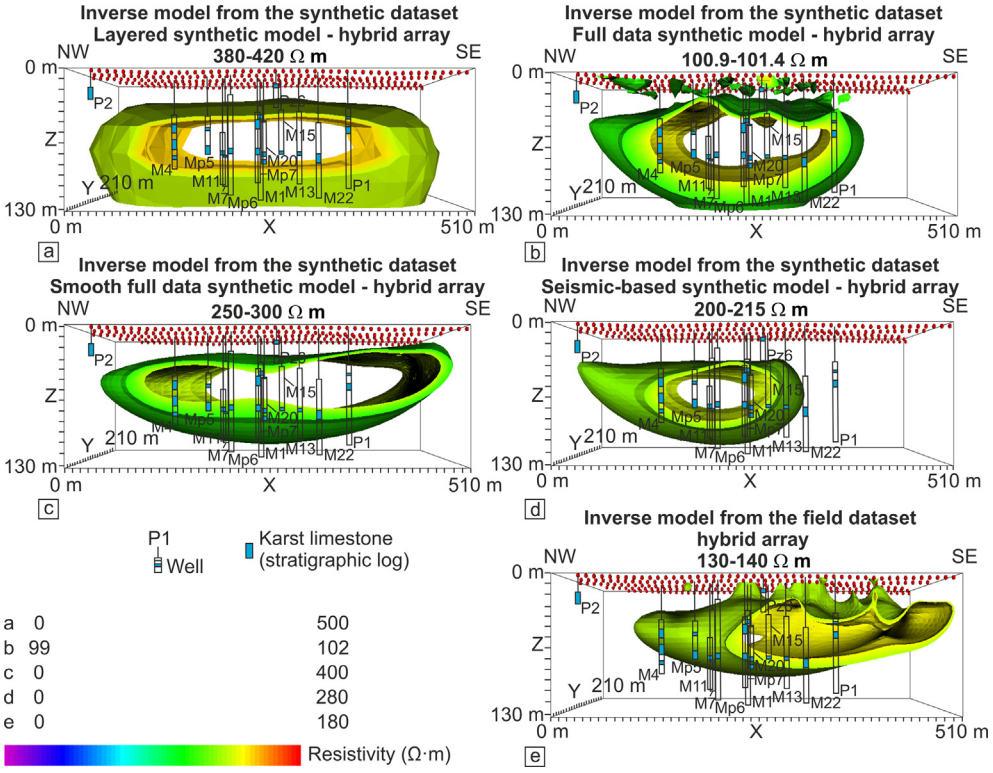

Fig. 8. Pseudo 3-D inverse resistivity models derived from synthetic datasets (a-d) through the application of the synthetic models (SYMs) with a variable degree of heterogeneity shown in Fig. 6: the resistivity range extractions seem to reproduce a better imaging of the first two main karst intervals occurring at depths of approximately 35–40 m and 85–87 m, as indicated by stratigraphic logs. The pseudo 3-D inverse model derived from the field dataset ((e), to facilitate comparison) is quite consistent with synthetic model results in identifying and imaging karst intervals. The models shown in (a, b, c, d, e) are 28.6%, 57.2%, 78.6%, 54% and 85.7%, respectively, consistent with stratigraphic logs in identifying karst intervals. The red dots included in the models represent the electrodes. Black shadows represent the innermost regions of the model. (For interpretation of the references to colour in this figure legend, the reader is referred to the web version of this article.)

the Y axis rather than from the 3-D sensitivity of the dataset. The use of an electrode spacing of 10 m along the X axis, although implying low resolution for identifying small structures at shallow depths, provides a suitable resolution for solving larger and deeper geophysical targets, considering that detectability falls as depth increases. However, the use of large-sized inversion elements may have led to a loss of resolution even along the X axis. Given the resolution provided by the experimental and inversion setup, the pseudo 3-D model is able to identify structures several meters in size: consequently, the karst bodies identified by the pseudo 3-D model represent, actually, broad high-porosity zones (i.e., several meters in size, as revealed by the study on the detectability of the geophysical model), rather than meter-scale, main zones of void development (35–40 m and 85–87 m deep), as identified by well logs.

The simplified conceptual model of the HES karst aquifer is shown in Fig. 9. This model represents the main features of the aquifer as revealed by well data and the pseudo 3-D ERT model.

A rough estimate of total porosity values for karst bodies can be obtained from the pseudo 3-D model by using the empirical relationship proposed by Archie (1942)

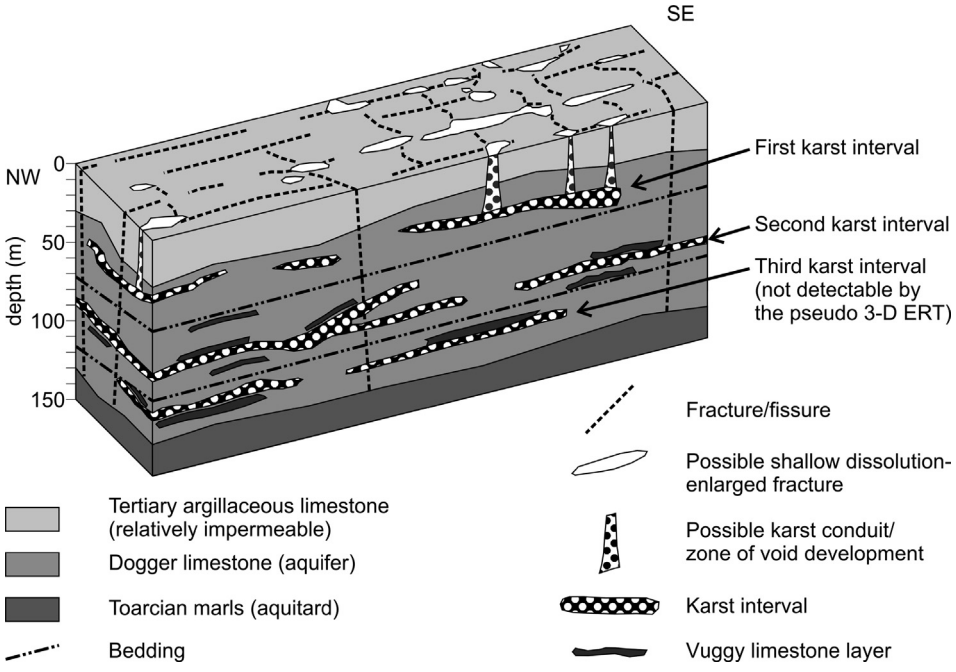

Fig. 9. Block diagram showing the simplified hydrogeological conceptual model of the HES karst aquifer, as revealed by well data and the pseudo 3-D ERT model.

$$\frac{R}{Rw} = F = \Phi^{-m} \quad (1)$$

where R = the resistivity of the true formation, Rw = the resistivity of the water impregnating the formation, F = the formation factor, Φ = the total porosity of the formation, m = the cementation factor, by using m = 2 and Rw = 20 Ω·m, i.e., the mean resistivity value of groundwater samples collected from wells.

Although the applicability of Archie's law may be argued and is questionable for a karst reservoir, two reasons motivated its adoption. The first is that the reservoir can be regarded as being equivalent to a sedimentary carbonate formation at the resistivity imaging resolution scale: indeed, the pseudo 3-D ERT model shows a rather large-sized 27.1 m^3 element volume. Furthermore, the volume of the karst bodies represents only 2–3% of the reservoir volume (from borehole image analysis, Audouin, 2007).

Low-medium limestone resistivity volumes are found to correspond to hydraulically-conductive levels and zones, as identified from well-logging and flow interference tests (Audouin, 2007; Audouin et al., 2008). Differently, high limestone resistivity volumes are found to correspond to tight limestone. Bulk total porosity values of 38–39% and 19–20% obtained from the hybrid model (Fig. 5c) would represent karst bodies and tight limestone, respectively. In view of the ERT underestimation of the limestone bulk resistivity, with respect to the resistivity logs of wells, a possible overestimation of the total porosity (by ~3%) of karst and non-karst limestone should be considered. Mari et al. (2009) suggest that the bodies showing a total porosity of approximately 16% would represent tight limestone with a low permeability (less than a millidarcy) but nonetheless significant storability.

5. Conclusions

The resistivity imaging of the HES karst aquifer of Poitiers from pseudo 3-D ERT has been presented in this work. The pseudo 3-D model provided a good definition of the main hydrogeological units and structures such as karst intervals, possible shallow dissolution-enlarged fractures and likely soil-mantled, incipient sinkhole formation features.

The opportunity to cross-validate geophysical results with extensive ground truth available at the HES provided the accuracy of the pseudo 3-D model and the effectiveness of some of the most common surface electrode arrays in investigating difficult geological targets such as karst aquifers.

The detectability of karst intervals provided by the pseudo 3-D ERT model was assessed through synthetic dataset modelling. This approach also allowed an estimation of the response of the experimental and inversion set-up to a variable degree of heterogeneity of the aquifer using well-log data as geological *a priori* information and, therefore, allowing the interpretation of field data to be guided.

These findings may provide further insights on pseudo 3-D ERT's applicability and effectiveness in karst aquifer investigation and may be useful in survey designing and interpreting stages of ERT investigations aimed at imaging difficult geological targets such as karst aquifers.

6. Article impact statement

Pseudo 3-D ERT applicability and effectiveness in karst aquifer investigation.

Conflict of interest

None

Declaration of Competing Interest

The author declares that they have no known competing financial interests or personal relationships that could have appeared to influence the work reported in this paper.

Acknowledgements

The author wishes to thank Jean-Luc Mari (Institut Français du Pétrole Energies Nouvelles, Rueil-Malmaison, France), Gilles Porel (CNRS IC2MP UMR 7285, Université de Poitiers, France), Mario Luigi Rainone and Patrizio Signanini (INGEO, Università "G. d'Annunzio" di Chieti-Pescara, Italy) for very useful discussions, Pasquale Greco and Fabio Colantonio for their precious support and assistance, Bernard Bourbiaux, Benoît Nauleau, Denis Paquet, (CNRS IC2MP UMR 7285, Université de Poitiers, France), Martina Malandra, Giuliano D'Elia, Stefano Scialpi for the precious collaboration during data collection, Lorenzo Curato and Simone Trussardi for the precious collaboration during data editing. The author wishes to thank the Associate Editor Barbara Mahler and two anonymous referees who kindly reviewed the earlier version of this manuscript and provided valuable suggestions and comment. The author wishes also to thank Bertie Vitry for the proofreading of the manuscript.

Appendix A. Supplementary data

Supplementary data to this article can be found online at https://doi.org/10.1016/j.jhydrol.2019.124257.

References

Al-Zoubi, A.S., Abd El-Rahman, A.A., Al-Rzouq, R., Camerlynck, C., Akkawi, E., Ezersky, M., Abu-Hamatteh, Z.S.H., Ali, W., Al Rawashdeh, S., 2007. Use of 2-D multi electrodes resistivity imaging for sinkholes hazard assessment along the Eastern part of the Dead Sea, Jordan. Am. J. Environ. Sci. 3 (4), 229–233.

Arato, A., Godio, A., Sambuelli, L., 2014. Staggered grid inversion of cross hole 2-D resistivity tomography. J. Appl. Geophys. 107, 60–70.

Archie, G.E., 1942. The electrical resistivity log as an aid in determining some reservoir characteristics. J. Petrol. Technol. 1, 55–62.

Athanasiou, E.N., Tsourlos, P.I., Papazachos, C.B., Tsokas, G.N., 2007. Combined weighted inversion of electrical resistivity data arising from different array types. J. Appl. Geophys. 62 (2), 124–140.

Audouin, O., 2007. Intégration - inversion de données géologiques et mesures hydrodynamiques in-situ pour le conditionnement d'un modèle 3-D d'aquifère calcaire: Site Expérimental Hydrogéologique (SEH) de Poitiers, France. PhD thesis. University of Nottingham.

Audouin, O., Bodin, J., 2007. Analysis of slug-tests with high-frequency oscillations. J. Hydrol. 334, 282–289.

Audouin, O., Bodin, J., 2008. Cross-borehole slug test analysis in a fractured limestone aquifer. J. Hydrol. 348, 510–523.

Audouin, O., Bodin, J., Porel, G., Bourbiaux, B., 2008. Flowpath structure in a limestone aquifer: multi-borehole logging investigations at the hydrogeological experimental site of Poitiers, France. Hydrogeol. J. 16 (5), 939–950.

Bernard, S., Delay, F., 2008. Determination of porosity and storage capacity of a calcareous aquifer (France) by correlation and spectral analyses of time series. Hydrog. J. 16, 1299–1309.

Bernard, S., Delay, F., Porel, G., 2006. A new method of data inversion for the identification of fractal characteristics and homogenization scale from hydraulic pumping tests in fractured rocks. J. Hydrol. 328 (3–4), 647–658.

Bourbiaux, B., Callot, J.-P., Doligez, B., Fleury, M., Gaumet, F., Guiton, M., Lenormand, R., Mari, J.-L., Pourpak, H., 2007. Multi-Scale Characterization of an Heterogeneous Aquifer Through the Integration of Geological, Geophysical and Flow Data: a Case Study. Oil & Gas Sci. Technol. 62 (3), 347–437.

Burbaud-Vergneaud, M., 1987. Fracturation et interactions soclecouverture: le Seuil du Poitou [Fractures and bedrock sedimentary cover interactions: Seuil du Poitou]. PhD Thesis. University of Poitiers, France.

Buvat, S., Schamper, C., Tabbagh, A., 2013. Approximate three-dimensional resistivity modelling using Fourier analysis of layer resistivity in shallow soil studies. Geophys. J. Int. 194 (1), 158–169.

Carrière, S.D., Chalikakis, K., Sénéchal, G., Danquigny, C., Emblanch, C., 2013. Combining Electrical Resistivity Tomography and Ground Penetrating Radar to study geological structuring of karst Unsaturated Zone. J. Appl. Geophys. 94, 31–41.

Cassiani, G., Godio, A., Stocco, S., Villa, A., Deiana, R., Frattini, P., Rossi, M., 2009. Monitoring the hydrologic behaviour of a mountain slope via time-lapse electrical resistivity tomography. Near Surf. Geophys. 7, 475–486.

Dahlin, T., Loke, M.H., 1998. Resolution of 2-D Wenner resistivity imaging as assessed by numerical modelling. J. Appl. Geophys. 38, 237–249.

Daily, W., Owen, E., 1991. Crosshole resistivity tomography. Geophysics 56, 1228–1235.

Daily, W., Ramirez, A., 1992. Electrical resistivity tomography of vadose water movement. Water Resour. Res. 28, 1429–1442.

De Dreuzy, J.R., Bodin, J., Le Grand, H., Davy, P., Boulanger, D., Battais, A., Bour, O.,

Gouze, P., Porel, G., 2006. General Database for Ground Water Site Information. Ground Water 44 (5), 743–748.
Delay, F., Porel, G., Bernard, S., 2004. Analytical 2-D model to invert hydraulic pumping tests in fractured rocks with fractal behavior. Geophys. Res. Letters 31, L16501. https://doi.org/10.1029/2004GL020500.
Delay, F., Kaczmaryk, A., Ackerer, P., 2007. Inversion of interference hydraulic pumping tests in both homogeneous and fractal dual media. Adv. Water Resour. 30 (3), 314–334.
Griffiths, D.H., Barker, R.D., 1993. Two-dimensional resistivity imaging and modeling in areas of complex geology. J. Appl. Geophys. 29, 211–226.
Guérin, R., Benderitter, Y., 1995. Shallow karst network exploration using MT-VLF and DC resistivity methods. Geophys. Prospect. 43 (5), 635–653.
Guérin, R., Bégassat, P., Benderitter, Y., David, J., Tabbagh, A., Thiry, M., 2004. Geophysical study of the industrial waste land in Mortagne-du-Nord (France) using electrical resistivity. Near Surf. Geophys. 2 (3), 137–143.
Kaczmaryk, A., Delay, F., 2007a. Interference pumping tests in a fractured limestone (Poitiers - France): inversion of data by means of dual-medium approaches. J. Hydrol. 337 (1–2), 133–146.
Kaczmaryk, A., Delay, F., 2007b. Improving dual-porosity medium approaches to account for karst flow in a fractured limestone: application to the automatic inversion of hydraulic interference tests (Hydrogeological Experimental Site, HES - Poitiers - France). J. Hydrol. 347 (3–4), 391–403.
Kuras, O., Pritchard, J.D., Meldrum, P.I., Chambers, J.E., Wilkinson, P.B., Ogilvy, R.D., Wealthall, G.P., 2009. Monitoring hydraulic processes with Automated time-Lapse Electrical Resistivity Tomography (ALERT). Comptes Rendus Geoscience - Special Issue on Hydrogeophysics 341, 868–885.
LaBrecque, D.J., Miletto, M., Daily, W., Ramirez, A., Owen, E., 1996. The effects of noise on Occam's Inversion of resistivity tomography data. Geophysics 61, 538–548.
Loke, M.H., Acworth, I., Dahlin, T., 2003. A comparison of smooth and blocky inversion methods in 2-D electrical imaging surveys. Explor. Geophys. 34, 182–187.
Maillol, J.M., Seguin, M.-K., Gupta, O.P., Akhauri, H.M., Sen, N., 1999. Electrical resistivity tomography survey for delineating uncharted mine galleries in West Bengal, India. Geophys. Prospect. Eur. Assoc. Geosci. Eng. 47, 103–116.
Mari, J.L., Delay, F., 2011. Contribution of seismic and acoustic methods to reservoir model building, Hydraulic Conductivity-Issues, Determination and Applications. InTech 329–354.
Mari, J.L., Porel, G., 2008. 3-D Seismic Imaging of a Near-Surface Heterogeneous Aquifer: A Case Study. Oil Gas Sci. Technol. Rev, IFP 63 (2), 179–201.
Mari, J.L. and Porel, G., 2008b. From 3-D seismic and resistivity logs to 3-D porosity: the case study of a near-surface heterogeneous aquifer. In: 70th EAGE Conference, 9-12 June 2008, Rome. Extended Abstract, D037.
Mari, J.-L., Porel, G., Bourbiaux, B., et al., 2009. From 3D Seismic to 3D Reservoir Deterministic Model Thanks to Logging Data: the Case Study of a Near Surface Heterogeneous Aquifer. Oil & Gas Sci. Technol. 1–13. https://doi.org/10.2516/ogst:2008049.
Meyerhoff, S.B., Karaoulis, M., Fiebig, F., Maxwell, R.M., Revil, A., Martin, J.B., Graham, W.D., 2012. Visualization of conduit-matrix conductivity differences in a karst aquifer using time-lapse electrical resistivity. Geophys. Res. Lett. 39, L24401. https://doi.org/10.1029/2012GL053933.
Meyerhoff, S.B., Maxwell, R.M., Revil, A., Martin, J.B., Karaoulis, M., Graham, W.D., 2014. Characterization of groundwater and surface water mixing in a semiconfined karst aquifer using time-lapse electrical resistivity tomography. Water Resour. Res. 50, 2566–2585. https://doi.org/10.1002/2013WR013991.
Morelli, G., LaBrecque, D.J., 1996. Advances in ERT inverse modelling. Eur. J. Environ. Eng. Geophys. Society 1 (2), 171–186.
Rainone, M.L., Rusi, S., Torrese, P., 2015. Mud Volcanoes in Central Italy: Subsoil Characterization through a Multidisciplinary Approach. Geomorphology 234, 228–242.
Ritz, M., Robain, H., Pervago, E., Albouy, Y., Camerlynck, C., Descloitres, M., Mariko, A., 1999. Improvement to resistivity pseudosection modelling by removal of near-surface heterogeneity effects: application to a soil system in South Cameroon. Geophys. Prospect. 47, 85–101.
Saribudak, M. and Hawkins, A., 2019. A geophysical attempt to locate a potential cave in the near-vicinity of a water well at Anacacho Limestone setting, Medina County, Texas. Bulletin of the South Texas Geological Society LIX(6), 1-11.
Satitpittakul, A., Vachiratienchai, C., Siripunvaraporn, W., 2013. Factors influencing cavity detection in Karst terrain on two-dimensional (2-D) direct current (DC) resistivity survey: a case study from the western part of Thailand. Eng. Geol. 152 (1), 162–171.
Smith, D.L., 1986. Application of the pole–dipole resistivity technique to the detection of solution cavities beneath highways. Geophysics 51 (3), 833–837.
Spiegel, R.J., Sturdivant, V.R., Owen, T.E., 1980. Modeling resistivity anomalies from localized voids under irregular terrain. Geophysics 45, 1164–1183.
Szalai, S., Novák, A. and Szarka, L., 2009. Depth of Investigation and Vertical Resolution of Surface Geoelectric Arrays. J. Environ. Eng. Geophys. 14 (1), 15–23.
Van Schoor, M., 2002. Detection of sinkholes using 2-D electrical resistivity imaging. J. Appl. Geophys. 50 (4), 393–399.
Zhu, J., Currens, J.C., Dinger, J.S., 2011. Challenges of using electrical resistivity method to locate karst conduits - a field case in the Inner Bluegrass Region, Kentucky. J. Appl. Geophys. 75 (3), 523–530.